Fractal Weyl law for three-dimensional chaotic hard-sphere scattering systems

Alexander Eberspächer, Jörg Main, and Günter Wunner

Institut für Theoretische Physik 1, Universität Stuttgart, 70550 Stuttgart, Germany

(Dated: August 5, 2010)

The fractal Weyl law connects the asymptotic level number with the fractal dimension of the chaotic repeller. We provide the first test for the fractal Weyl law for a three-dimensional open scattering system. For the four-sphere billiard, we investigate the chaotic repeller and discuss the semiclassical quantization of the system by the method of cycle expansion with symmetry decomposition. We test the fractal Weyl law for various symmetry subspaces and sphere-to-sphere separations.

I. INTRODUCTION

The asymptotic eigenvalue distribution of partial differential equations such as the Schrödinger equation for free particles or the one-dimensional Helmholtz equation for sound waves has been of interest as early as from 1912 on when Hermann Weyl and Richard Courant first studied the problem [1, 2]. They found expressions for the asymptotic level number $N(k)$ in closed systems to be proportional to k^d, with d the spatial dimension of the system. The so called "Weyl law", which has been well known from then on [3], states that for *closed* quantum systems, every accessible Planck cell in phase space is occupied by one quantum state. A generalization to chaotic *open* systems, where complex resonances $k_n = \bar{k}_n - \Gamma_n/2$ with mean energies k_n and lifetimes Γ_n replace real eigenvalues k, has been proposed in the 1990s [4, 5]. The number of resonances

$$N(k) = \{k_n \colon \text{Re}(k_n) \le k; \text{Im}(k_n) > -C\} \qquad (1)$$

inside a rectangle in the complex plane defined by the energy k and the strip width C is conjectured to be proportional to k^α with the exponent

$$\alpha = \frac{D+1}{2} \qquad (2)$$

being related to the non-integer fractal dimension D of the *chaotic repeller*. The number α takes the role of the effective number of degrees of freedom. The repeller is the set of all classical trajectories that stay trapped for $t \to +\infty$ or $t \to -\infty$. Considering only the stable manifold $\mathcal{W}_\text{s}$ of trapped trajectories for $t \to +\infty$ in a suitable Poincaré surface of section, the fractal Weyl law reads [6]

$$N(k) \propto k^{d_\text{H}+1}, \qquad (3)$$

with d_H the Hausdorff dimension of the chaotic repeller's stable manifold.

The fractal Weyl law (3) has been investigated for various two-dimensional systems, e.g. a triple Gaussian potential [7], the three-disk billiard [6], an optical microstadium resonator [8] and a modified Hénon-Heiles potential
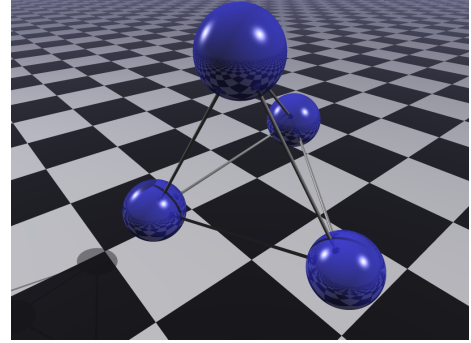

FIG. 1. The four-sphere billiard. Four spheres of equal radius R are located on the vertices of an equilateral tetrahedron (indicated by bars) with edge length d. Shown is the case of $d/R = 6$.

[9] as well as for quantum maps, e.g. the kicked rotator [10, 11]. The systems under consideration so far have all been at most two-dimensional. We provide a first investigation of a three-dimensional system in this paper.

The problem under consideration is scattering in the four-sphere billiard. This system is characterized by four spheres of the same radius R located on the vertices of an equilateral tetrahedron with edge length d as visualized in Fig. 1. The relevant configuration parameter is the ratio d/R. Different from e.g. the two-dimensional three-disk billiard, the four-sphere billiard is an open system even for the case of touching spheres at $d/R = 2$.

The paper is organized as follows. The fractal dimension of the repeller is computed in Sec. II. Periodic-orbit theory and cycle expansion methods are applied in Sec. III to obtain semiclassical resonance spectra. The classical escape rate is determined in Sec. IV. Results which allow for a test of the fractal Weyl law are presented in Sec. V. Concluding remarks are given in Sec. VI.

II. GAUGING THE REPELLER

As the fractal dimension D of the chaotic repeller enters into the fractal Weyl law (3), it is crucial to determine D accurately. The fractal structures in the four-

sphere billiard have already been studied experimentally and theoretically [12–15], however, all investigations so far have been limited to small values of the configuration parameter $d/R \lesssim 2.5$. In this paper the fractal dimension of the repeller is determined accurately for a wide range of the parameter d/R.

A. Fractal repeller

The stable manifold $\mathcal{W}_{\mathrm{s}}$ of the chaotic repeller is a fractal in phase space. The time spent in the scattering system can be measured by the time-delay function T counting the number of reflections experienced by a trajectory. Choosing initial conditions in a plane parallel to the plane spanned by three of the spheres, it is possible to iterate trajectories entering the scattering system such that the fourth sphere is visited first. For large ratios d/R, the boundary to the region that contains those initial conditions is the projection of the fourth sphere onto the plane from which the trajectories are iterated. As there are three distinct possibilities to visit the next sphere, there are three regions of higher values of T inside this circle. Repeating this line of argument for any region belonging to a given visitation sequence, the structure of the fractal repeller can be understood. Figure 2 illustrates the fractal structure.

In principle, the Hausdorff dimension d_{H} can be calculated from box-counting. This procedure, however, is not suited for the billiards under consideration as it requires iteration of a vast amount of initial conditions on a grid. The regions of high values of T that exhibit fractal properties may not be resolved with acceptable computational effort. A method better suited to billiards is introduced below.

B. Estimating d_{H} through Hausdorff sums

Finite numerical precision and finite computing time available prevent the determination of initial conditions that lead to trapped orbits. Instead, it is possible to estimate the Hausdorff dimension from regions of finite T. We introduce the auxiliary quantity $A_n^{(i)}$ that denotes the area of the n-th region of initial conditions with $T \geq i$ reflections in the surface of section, and define the quantities

$$K^{(i)}(s) := \sum_n \left(A_n^{(i)} \right)^s \qquad (4)$$

which will be called Hausdorff sums below. These sums have the following properties [16, 17]:

$$\lim_{i \to \infty} K^{(i)}(s) = \begin{cases} \infty & \text{for } 0 \leq s < d_{\mathrm{H}} \\ \text{const.} > 0 & \text{for } s = d_{\mathrm{H}} \\ 0 & \text{for } d_{\mathrm{H}} < s < \infty \end{cases} \qquad (5)$$
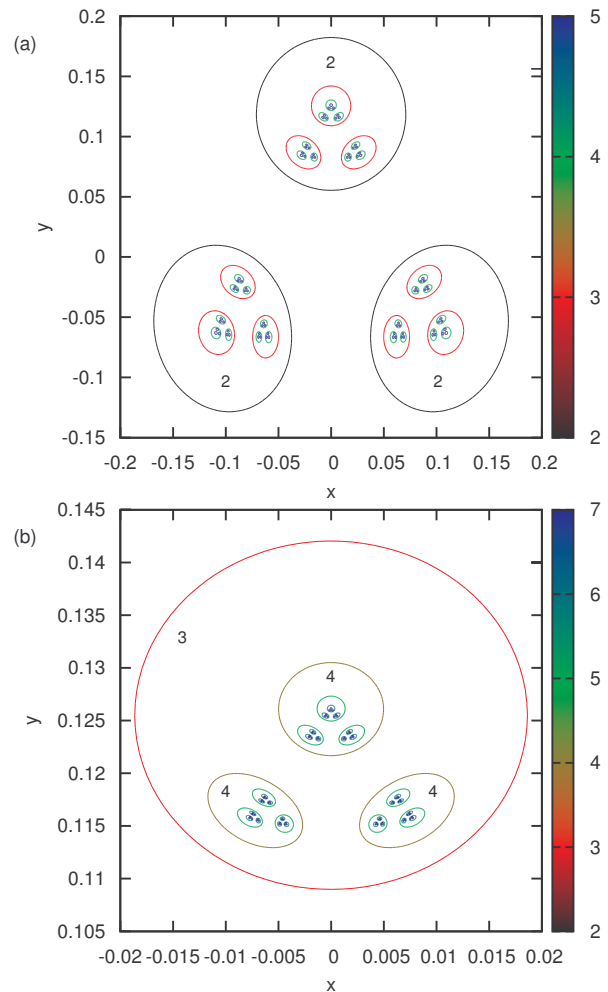

FIG. 2. (a) Time-delay functions in the range $2 \leq T \leq 5$ for $d/R = 3$ and (b) a magnification thereof in the range $2 \leq T \leq 7$. The time-delay functions are drawn as functions of the coordinates x, y in the surface of section. The colors indicate the value of T and for clear identification some regions are explicitly labeled with T. Only the boundaries of individual regions are drawn; initial conditions chosen within the regions experience the same number of reflections. The self-similarity suggests that the stable manifold is a fractal set.

The property for $s = d_{\mathrm{H}}$ stems from the fact that the Hausdorff sums by definition are smooth functions of the variable s. This allows one to estimate the Hausdorff dimension d_{H} by intersecting $K^{(i)}(s)$ for different i [14, 15].

Existing methods of estimating the repeller's fractal dimension have been confined to a narrow range of the parameter d/R, in particular to the case of almost-touching spheres [14, 15]. The algorithm discussed in the following allows for calculations in a wider range of d/R. To estimate the stable manifold $\mathcal{W}_{\mathrm{s}}$ in the surface of initial conditions, it will be necessary to accurately find boundaries of regions of a given visitation sequence of the spheres and reflection count. Once both a point inside the region in question and a point outside are known, interval bi-

section may be used to compute the boundary point on the line connecting both points. The bisection condition uses the visitation sequence and the reflection count T, i.e. the length of the symbolic code.

1. Finding regions

The algorithm used in this paper relies on the structure of the time-delay functions discussed in Sec. II A. In the calculations, the following assumptions are made:

- Regions of a specific order of visits with the scatterers described by the symbolic code are non-overlapping.

- Within a region of a given order of visits, there are exactly three more regions each corresponding to additional visits at one of the three other spheres.

Both conditions may be violated for d/R close to 2, i.e. the case of almost touching spheres. We find the assumptions to be fulfilled for regions with $T \geq 2$ and configurations $d/R \gtrsim 2.5$.

All steps of the procedure are based on the Poincaré surface of section chosen such that iteration starts from a plane parallel to the plane spanned by the three closest spheres. The velocities are chosen parallel to the z-axis such that the uppermost sphere is visited first. Let us assume that regions with $T_{\min} \leq T \leq T_{\max}$ are sufficient for an estimation of d_{H}. Under this assumption, it is possible to find regions approximating the repeller with the following procedure.

In the a first step, the projection of the sphere visited first onto the surface of section is determined. For small d/R, this region is a circle, for larger d/R, projections of the other spheres may be cut out of the circle. This is done by randomly choosing a point in the surface of section and an interval bisection between this point and points equally distributed on a large circle fully containing the projection of sphere 4. By assumption, inside this region there are three other regions with $T = 2$. The corresponding visitation sequences differ in the second character. Once a point inside each of the regions with $T = 2$ is found, in a second step, polygonal chains forming boundaries to each of the new distinct regions are calculated. This procedure is iterated until all desired regions corresponding to $T_{\min} \leq T \leq T_{\max}$ have been found.

2. Areas from polygonal chains

One possibility to store the boundaries is by keeping a polygonal chain. As in this procedure the number N_{regions} of regions grows exponentially with $N_{\mathrm{regions}} = 3^{T-1}$, this way of data storage is memory-expensive. However, the areas enclosed by the polygons are easily

TABLE I. Numerical values of the Hausdorff dimensions d_{H} of the stable manifold $\mathcal{W}_{\mathrm{s}}$ for various configuration parameters d/R. All decimal digits are significant.

d/R	2.5	3	4	5	6	8	10
d_{H}	0.4774	0.3818	0.2992	0.2596	0.2354	0.2063	0.1888

calculated using numerical quadrature of the area given by

$$A = \frac{1}{2} \int_0^{2\pi} r^2(\varphi)\, \mathrm{d}\varphi\,, \qquad (6)$$

with $r(\varphi)$ the distance of the boundary point from the "midpoint" of the region. A fairly low number of supporting points has proved to be sufficient for very high precision. All calculations have been performed with 101 supporting points.

3. Areas from ellipses

An alternative to the memory-expensive storage of polygonal chains is to approximate the boundary by an ellipse described by the polynomial

$$a_1 x^2 + a_2 y^2 + a_3 xy + a_4 x + a_5 y = 1\,. \qquad (7)$$

For five or more known points (x_i, y_i) of the boundary the coefficients $a_1, \ldots, a_5$ can be determined from a linear least-squares fit. The semi-major axes a, b, the center shift (x_0, y_0) as well as the rotation angle φ of the ellipses can be easily extracted from the coefficients of the polynomial in Eq. (7).

Fitted ellipses allow to improve accuracy as it is now possible to shift the regions' "midpoints" used in the construction of the polygonal chains to the midpoint of the ellipses. All bisections for the polygonal chain boundaries are repeated in such a way that all lines connecting the ellipse's midpoints and the boundary points intersect at identical angles. This will be beneficial for the quadrature of the areas entering into the Hausdorff sums.

Once all desired boundaries have been calculated, the fractal dimension d_{H} can be estimated. To build the Hausdorff sums (4), the areas enclosed in the individual regions have to be known. From the ellipses fitted to the boundaries, the area A is trivially given by

$$A = \pi a b\,, \qquad (8)$$

where a and b are the semi-major axes.

Calculations have been performed for $d/R = 2.5$ to $d/R = 10$. Sample plots for intersected Hausdorff sums $K^{(i)}(s)$ are shown in Fig. 3. Results for the Hausdorff dimension d_{H} are compiled in Fig. 4 and in Table I. The calculations using polygonal chains agree up to four decimal digits with the calculations using fitted ellipses.
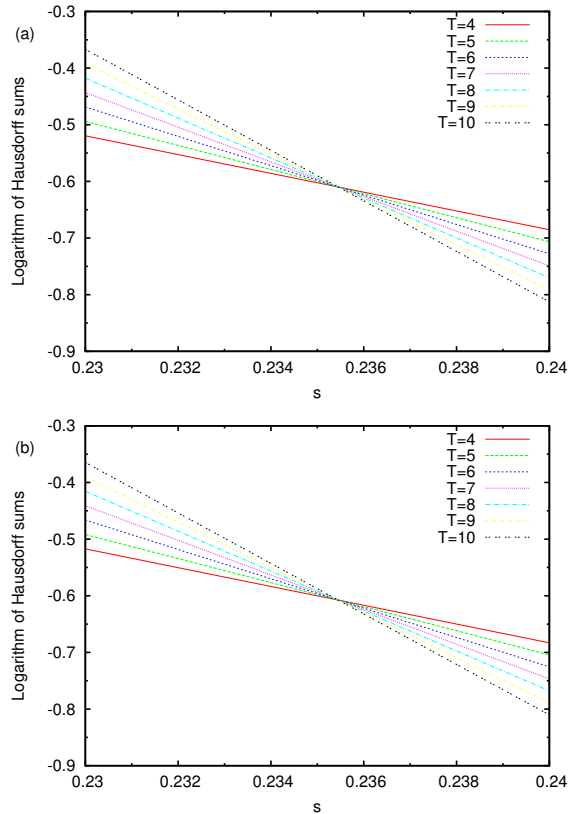
FIG. 3. Intersected Hausdorff sums $K^{(i)}(s)$ for various reflection numbers $i = T$ calculated from (a) a polygonal chain with 101 supporting points and (b) ellipses fitted to polygonal chains for $d/R = 6$. As can clearly be seen, the intersection points for all shown curves agree perfectly. For this reason, the Hausdorff dimensions can be determined to a precision of at least 4 significant digits.

Figure 4 clearly shows that with decreasing d/R the intersection of the stable manifold $\mathcal{W}_s$ with the Poincaré surface of section fills the plane denser. The repeller's dimension d_H thus increases as the tetrahedron gets packed more densely.

In summary, the method presented here establishes a fast and very precise method of gauging the repeller. Though the assumptions are quite strong, they hold over a wide range of the ratio d/R.

III. SEMICLASSICAL RESONANCES

Studying a billiard system in a purely quantum mechanical fashion turns out to be intricate since – although particles move freely in between the scatterers – it is a demanding task to find wavefunctions that vanish on all scatterer's boundaries simultaneously. For attempts on N-sphere scattering systems in three dimensions, see [18]; for the two-dimensional three-disk scattering system see [19]. Results and comparisons of methods for the four-sphere scattering system are presented in [20]. The tech-
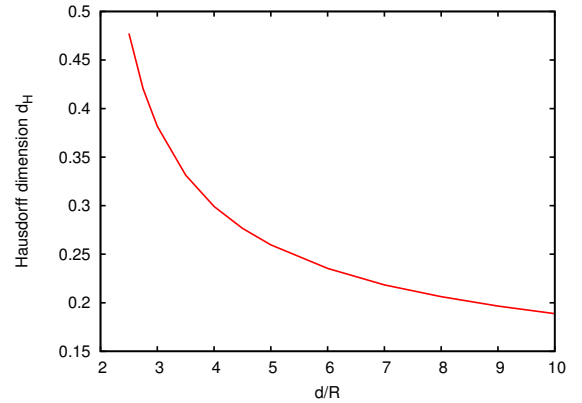

FIG. 4. Hausdorff dimension d_H of the stable manifold $\mathcal{W}_s$ as function of the ratio d/R. All data points have been obtained by intersecting Hausdorff sums as demonstrated in Fig. 3.

niques of *semiclassical quantization* presented below are better suited for billiard systems.

As one of the great achievements of semiclassical physics, Gutzwiller's trace formula provides a mean of quantizing a system via periodic orbits [21]. Unfortunately, the trace formula is plagued by serious convergence problems. In chaotic systems, the number of periodic orbits typically grows exponentially with length l, and this growth usually cannot be compensated by the decrease of the amplitude factors. A method of improving the convergence ideally suited for billiard systems is based on the Gutzwiller-Voros zeta function.

The logarithmic derivative of the function

$$Z(k) = \prod_n (k - k_n) \tag{9}$$

with the quantized wavenumbers k_n of a billiard system yields the density of states

$$g(k) = -\frac{1}{\pi} \operatorname{Im} \frac{\mathrm{d}}{\mathrm{d}k} \ln Z(k) = -\frac{1}{\pi} \operatorname{Im} \sum_n \frac{1}{k - k_n + \mathrm{i}\epsilon} . \tag{10}$$

Voros [22] proposed a semiclassical formulation of $Z(k)$ which reads for billiard systems

$$Z_{\mathrm{GV}}(k) = \exp\left(-\sum_p \sum_{r=1}^{\infty} \frac{1}{r} \frac{(-1)^{rn_p} \, \mathrm{e}^{\mathrm{i}rl_p k}}{\sqrt{|\det(\boldsymbol{M}_p^{\ r} - \boldsymbol{1})|}} \right) , \tag{11}$$

where l_p is the length of a primitive periodic orbit and n_p the number of reflections on hard wall boundaries. The index r counts the number of repetitions of a primitive periodic orbit. The reduced monodromy matrix $\boldsymbol{M}_p$ provides information on the linear evolution of a small deviation from an initial condition belonging to a periodic orbit over one period [23]. The eigenvalues of $\boldsymbol{M}_p$ quantify the stability of the periodic orbit. Due to the symplectic structure of Hamiltonian mechanics, the eigenvalues come in tuples λ, $1/\lambda$, λ^*, and $1/\lambda^*$.

TABLE II. Character table for the group T_d [20]. The group has five irreducible representations: the one-dimensional representations A_1 and A_2, the two-dimensional representation E and the two three-dimensional representations T_1 and T_2.

T_d	E	$8C_3$	$3C_2$	$6S_4$	$6\sigma_d$
A_1	1	1	1	1	1
A_2	1	1	1	−1	−1
E	2	−1	2	0	0
T_1	3	0	−1	1	−1
T_2	3	0	−1	−1	1

For systems with symbolic dynamics such as billiards, the method of *cycle expansion* [24–27] has proved to be especially successful. A cycle expansion of the Gutzwiller-Voros zeta function $Z_{\mathrm{GV}}(k)$ in Eq. (11) is achieved by replacing $(-1)^{rn_p}$ in Eq. (11) by the term $(-z)^{rn_p}$ depending on the book-keeping variable z, expanding Z_{GV} as a power series in z and then truncating the series. The highest power of z equals the maximum cycle length $n_{\max}$ contributing to the cycle expansion. After truncation, z has to be set to $z = 1$. The cycle-expanded zeta function has better convergence behavior over the trace formulas as individual terms tend to cancel.

A.   The symmetry group T_d

The four-sphere billiard has discrete tetragonal symmetry [20]. The associated symmetry group T_d contains all symmetry operations that leave a regular tetrahedron invariant. In particular, there are the identity operation E, 4 rotations C_3 by $2\pi/3$ around the axes defined by a vertex of the tetrahedron and the center of the facing triangular boundary surface, 4 more rotations $C_3{}^2$ by $4\pi/3$ around the same axes, 3 rotations C_2 by π around the axes intersecting the middle points of opposing edges, 6 reflections σ_d at planes perpendicular to the tetrahedron's edges and also containing another vertex; and, furthermore, 3 permutations of the vertices S_4 which can be written as a combination of a rotation C_4 by $\pi/2$ and a reflection σ_h at the plane perpendicular to the main rotation axis, i.e. the axes of C_3. Finally, the symmetry group T_d also contains 3 distinct three-times repeated rotary reflections $S_4{}^3$.

The character table of the symmetry group is given in Table II. The symmetry group can be decomposed into 5 invariant subspaces, i.e. the representation matrices $\boldsymbol{D}$ of T_d can be decomposed into block-diagonal form where the diagonal elements contain matrices representing the group's elements. The representation is called "irreducible" if no further decomposition is possible.

From the character table, statements on the wavefunctions ψ can be made. For the one-dimensional representations A_1 and A_2, the effect of the symmetry transformations is described by a multiplication with the character χ. For the totally symmetric A_1 subspace, all characters are equal to 1, therefore the wavefunctions have the full symmetry of T_d, i.e. ψ is not altered by any symmetry transformation. In the A_2 subspace, the wavefunction changes sign under the reflection σ_d and permutation S_4. For representations of higher dimension, the effect of the symmetry transformations cannot be described in such a simple way.

We note that repeated application of symmetry transforms may be identical with other elements of the symmetry group, e.g., $\sigma_d{}^2 = C_2{}^2 = C_3{}^3 = S_4{}^4 = E$ and $S_4{}^2 = C_2$. These identities will be useful for the symmetry decomposition of zeta functions discussed below.

B.   Symbolic dynamics and periodic orbits in the four-sphere scattering system

The method of cycle expansion requires all periodic orbits up to a given maximum cycle length n_r. In special billiards it is convenient to assign a *symbolic code* to each periodic orbit. For the four-sphere scattering system the symbolic dynamics and periodic orbits have already been introduced in Ref. [20]. For the convenience of the reader we briefly recapitulate the central ideas and properties of the orbits.

In the four-sphere scattering system, periodic orbits are determined by the periodic sequence in which the four scatterers are visited. For most cases, any sequence corresponds to one periodic orbit. If this one-to-one correspondence is not given, i.e. if some orbits become unphysical because they penetrate the scatterers, one speaks of *pruning*. This is the case for small center-to-center separations. In the four-sphere scattering system, the symbolic dynamics has been shown to be pruned for configurations with $d/R < 2.0482$ [20].

1.   Periodic orbits in the fundamental domain

In systems with discrete symmetries such as the four-sphere billiard, which is invariant under all symmetry operations of the tetrahedron group T_d, whole classes of orbits are equivalent to each other, e.g., the 6 orbits which are scattered back and forth between two spheres can be mapped onto each other using symmetry operations of T_d. Furthermore, cyclic permutation of the sequence of spheres leaves the orbits invariant. For these reasons, it is appropriate to use the symmetry properties to introduce the following short notation [20]. First, define the plane of reflection as the plane that contains the centers of the last three distinct spheres visited. Then, instead of labeling all spheres individually, the label 0 will be used if the orbit visits the last sphere once more, 1 will indicate a visit at the third other sphere in the same plane of reflection, whereas the label 2 will be used for a visit at the fourth sphere outside the plane of reflection. With this nomenclature, all symbolic codes containing the charac-

TABLE III. Primitive periodic orbits up to cycle length $n_{\tilde{p}} = 2$ for $d/R = 4$. The reduced symbolic code $\tilde{p}$ as well as the symmetry $h_{\tilde{p}}$ of each cycle is given. Furthermore, the real and imaginary parts of the stability eigenvalues $\lambda_{\tilde{p}}^{(i)}$ are tabulated. All numbers have been rounded to five decimal digits. The shortest cycle, labeled by 0, which visits two spheres in turns has ambiguous symmetry. Both the rotation about π, C_2, as well as the reflection about the plane perpendicular to the line connecting the sphere's center, σ_d, map this particular orbit onto itself.

$\tilde{p}$	$h_{\tilde{p}}$	$l_{\tilde{p}}$	Re $\lambda_{\tilde{p}}^{(1)}$	Im $\lambda_{\tilde{p}}^{(1)}$	Re $\lambda_{\tilde{p}}^{(2)}$	Im $\lambda_{\tilde{p}}^{(2)}$
0	σ_d, C_2	2.00000	5.82843	0.00000	5.82843	0.00000
1	C_3	2.26795	-7.09669	0.00000	5.75443	0.00000
2	S_4	2.31059	-3.11111	5.69825	-3.11111	-5.69825
01	σ_d	4.34722	-46.21054	0.00000	32.08725	0.00000
02	C_3	4.35831	-14.95013	35.68205	-14.95013	-35.68205
12	S_4	4.58593	43.79192	0.00000	-39.51750	0.00000

ter 2 are three-dimensional, whereas orbits corresponding to sequences of 0 and 1 are two-dimensional. The new labeling reduces the number of characters in the alphabet to three, i.e. the code is ternary. This reduction corresponds to a reduction of the full physical phase space M to the fundamental domain $\tilde{M}$ from which the whole phase space can be reconstructed by applying the symmetry group's elements. Note that the symmetry reduced orbits are in general shorter than the corresponding physical ones. Only the symmetry reduced orbits that have the identity operation E as maximum symmetry have the same length as the corresponding physical orbits. The reduced orbits of symmetry classes σ_d and C_2 yield twice as long physical orbits, C_3 orbits are three times longer than in the physical space, and, finally, S_4 orbits have quadruple length.

2. Finding periodic orbits

Periodic orbits of the four-sphere scattering system are calculated by varying, for a given symbolic code, the reflection points on the spheres until the length of the orbit takes its minimum value. Details of the numerical periodic orbit search are described in [20] and the computation of the monodromy matrix is explained in Refs. [28, 29]. Table III lists the first few periodic orbits in the fundamental domain as well as their properties for the ratio $d/R = 4$. The table also gives the maximum symmetry operation that leaves the orbit invariant. In the fundamental domain, this operation corresponds to the operation that maps the endpoint of the orbit in the fundamental domain onto the starting point. Note that, for example, the cycle t_0 which visits two spheres in turns is periodic in the fundamental domain, but not in full physical space. In the full domain, the start and endpoint of the 0-cycle are not identical; application of the rotation C_2 respectively the reflection σ_d yields back the full periodic orbit.

C. Discrete symmetries and cycle expansion

In systems with discrete symmetries the full physical spectrum can be decomposed into spectra belonging to different representations of the symmetry group. The discrete symmetries lead to symmetry factorized zeta functions, which allow for the computation of quantum spectra belonging to a specific symmetry subspace. The symmetry decomposition of zeta functions has been elaborated by Cvitanović and Eckhardt [30] and examples have been given for the symmetry groups of various two-dimensional N-disk pinball models. Here, we present explicit results for the tetrahedron group T_d of the three-dimensional four-sphere scattering system. As in [30] we first discuss the symmetry decomposition of the dynamical zeta function

$$Z(k) = \prod_p \left(1 - t_p(k)\right) \tag{12}$$

which is obtained from the Gutzwiller-Voros zeta function (11) with the approximation

$$|\det(\boldsymbol{M}_p{}^r - \mathbf{1})|^{-1/2} \approx |\lambda_p^{(1)}\lambda_p^{(2)}|^{-r/2} = \mathrm{e}^{-(u_p^{(1)}+u_p^{(2)})r/2} \tag{13}$$

and the definition

$$t_p(k) = \mathrm{e}^{\mathrm{i}l_p k - (u_p^{(1)}+u_p^{(2)})/2} , \tag{14}$$

and then generalize the results for the symmetry decomposition of the Gutzwiller-Voros zeta function.

In quantum mechanics, the full Hilbert space $\mathcal{H}$ of the problem factorizes into subspaces belonging to certain irreducible representations of the symmetry group, i.e.

$$\mathcal{H} = \mathcal{H}_{A_1} \otimes \mathcal{H}_{A_2} \otimes \mathcal{H}_E \otimes \mathcal{H}_{T_1} \otimes \mathcal{H}_{T_2} , \tag{15}$$

for the four-sphere scattering system. In [30] it is pointed out that zeta functions can be factorized in a similar way. The fundamental domain of phase space is sufficient for all computations, as the whole phase space M can be obtained from the fundamental domain $\tilde{M}$ by

$$M = \sum_{h \in G} h\tilde{M} , \tag{16}$$

where G is the symmetry group. Evaluating traces of transfer operators in the fundamental domain $\tilde{M}$, this symmetry reduction results in [26, 30]

$$(1 - t_p)^{m_p} = \det\left(\mathbf{1} - \boldsymbol{D}\left(h_{\tilde{p}}\right) t_{\tilde{p}}\right) , \tag{17}$$

with m_p the multiplicity of a primitive cycle p.

These expressions could be evaluated using a certain explicit representation $\boldsymbol{D}_\alpha(h)$ of the group's symmetry operations h. However, this is a computationally rather

demanding endeavor. Instead, the determinants can be expressed in terms of traces χ which can be read off from the symmetry group's character table (see Table II). For example, the expansion of $\det(\mathbf{1} - \mathbf{D}(h)t)$ for dimension $d = 3$ reads

$$\det(\mathbf{1} - \mathbf{D}(h)t) = 1 - \chi(h)t + \frac{1}{2}\left(\chi(h)^2 - \chi\left(h^2\right)\right)t^2$$
$$+ \frac{1}{6}\left(\chi(h)^3 - 3\chi(h)\chi\left(h^2\right) + 2\chi\left(h^3\right)\right)t^3, \tag{18}$$

where the trace of $\mathbf{D}(h)$ is as usual denoted by $\chi(h)$. Carrying out this procedure explicitly, one obtains the factorizations given in Table IV. Thus, the zeta function in Eq. (12) can be rewritten in a symmetry reduced version

$$Z_\alpha = \prod_{\tilde{p}}(1 - \mathbf{D}_\alpha(h_{\tilde{p}})t_{\tilde{p}}) \tag{19}$$

for the subspace α. The zeta function now depends only on the fundamental cycles $\tilde{p}$. By this procedure, a factorization

$$Z(k) = \prod_\alpha Z_\alpha(k)^{d_\alpha} \tag{20}$$

is achieved. The zeta function Z factorizes into zeta functions belonging to certain irreducible representations α of the symmetry group. The dimensions d_α of the representations enter into the full zeta function – and with them, the quantum multiplicities of resonances belonging to a certain subspace.

1. Assigning weight factors

The method of cycle expansion expands the zeta function Z into a truncated series in which all cycles up to a certain cutoff length enter [24–27]. However, besides the primitive cycles, also multiple traversals contribute. Therefore, it needs to be clarified how repeated revolutions can be taken into account. Let us assume the primitive fundamental cycles $\tilde{p}$ are known. Then, the contribution of an r-times repeated revolution to the symmetry reduced zeta function (19) is given by polynomials such as

$$(1 - z^r t_{\tilde{p},r}), \tag{21}$$

where a dummy variable z has been introduced. The cycle weights $t_{\tilde{p},r}$ have the form of the terms in (11) and are thus easily calculable from the cycle weight $t_{\tilde{p}}$ of the primitive fundamental cycle. By using the factorizations given in Table IV, it is possible to determine the weight factor $w_{\tilde{p},r}(k)$ as the sum of all roots z_i^r of the polynomials given in the table,

$$w_{\tilde{p},r} = \sum_i z_i^r. \tag{22}$$

If this is possible, a way to use the $\tilde{p}$ for repetitions as well has been found. As an example, for the contribution of the r-times repeated cycle $\tilde{p}$ to the A_1 spectrum, we need to solve

$$(1 - z^r t_{\tilde{p},r}) = 0, \tag{23}$$

which is true for $z^r = 1$. Thus, in the A_1 subspace, all weight factors are $w_{\tilde{p},r} = 1$. By this choice, the symmetry factorization is retained. As another example, consider the E subspace for cycles with C_3 symmetry. Here, solutions to the equation

$$\left(1 + z^r t_{\tilde{p},r} + z^r t_{\tilde{p},r}{}^2\right) = 0 \tag{24}$$

are needed. A factorization is given by

$$\left(1 - e^{2\pi i r/3}\, t_{\tilde{p},r}\right)\left(1 - e^{-2\pi i r/3}\, t_{\tilde{p},r}\right) = 0, \tag{25}$$

where the exponentials are the roots z_i. Evaluating the sum $z_1^r + z_2^r$, we find the weight factors $w_{\tilde{p},r} = -1, -1, 2, -1, -1 \ldots$ for $r = 1, 2, \ldots$. A short notation for this sequence is given by $w_{\tilde{p},r} = 2\cos(2\pi r/3)$. By similar calculations, the weight factors $w_{\tilde{p},r}$ given in Table V are determined.

2. Ambiguous symmetry

The shortest cycle labeled by 0 in the four-sphere system has ambiguous symmetry. It is possible to map this cycle onto itself by both the rotation C_2 and the reflection σ_d. This ambiguity requires special care in the symmetry decomposition. This is particularly important as the 0-cycle is one of the fundamental cycles that act as building block for longer cycles in the sense of cycle expansion. The group theoretical weight of the 0-cycle can be written as [30]

$$h_0 = \frac{C_2 + \sigma_d}{2}. \tag{26}$$

The symmetry factorization can thus be not one of those given in Table IV. However, it is possible to use a factorization that contains factors in such a way that the factorization is at most the greatest common divisor of the factors given for C_2 and σ_d in Table IV. The factorizations and weight factors $w_{0,r}$ are given in Table VI. With that factorization the product (20) of all zeta functions belonging to the irreducible representations of the symmetry groups coincides with the cycle expansion (12) using all orbits in the full domain.

The final form of the Gutzwiller-Voros zeta function we use for our calculations is

$$Z_{\text{GV};\,\alpha}(k) = \exp\left(-\sum_{\tilde{p}}\sum_{r=1}^{\infty}\frac{1}{r}\frac{w_{\tilde{p},r;\alpha}(-z)^{rn_{\tilde{p}}}\, e^{i r l_{\tilde{p}} k}}{\sqrt{|\det(\mathbf{M}_{\tilde{p}}{}^r - \mathbf{1})|}}\right), \tag{27}$$

TABLE IV. Symmetry factorization of the zeta function Z for all five irreducible representations of the group T_d. The table entries give the contribution of each fundamental cycle $\tilde{p}$ to the Euler product $Z = \prod_{\tilde{p}}(1 - t_{\tilde{p}})$. This factorization allows the computation of quantum spectra for each symmetry subspace.

	E	C_3	C_2	S_4	σ_d
A_1	$(1 - t_{\tilde{p}})$	$(1 - t_{\tilde{p}})$	$(1 - t_{\tilde{p}})$	$(1 - t_{\tilde{p}})$	$(1 - t_{\tilde{p}})$
A_2	$(1 - t_{\tilde{p}})$	$(1 - t_{\tilde{p}})$	$(1 - t_{\tilde{p}})$	$(1 + t_{\tilde{p}})$	$(1 + t_{\tilde{p}})$
E	$(1 - t_{\tilde{p}})^2$	$(1 + t_{\tilde{p}} + t_{\tilde{p}}^2)$	$(1 - t_{\tilde{p}})^2$	$(1 - t_{\tilde{p}})(1 + t_{\tilde{p}})$	$(1 - t_{\tilde{p}})(1 + t_{\tilde{p}})$
T_1	$(1 - t_{\tilde{p}})^3$	$(1 - t_{\tilde{p}})(1 + t_{\tilde{p}} + t_{\tilde{p}}^2)$	$(1 - t_{\tilde{p}})(1 + t_{\tilde{p}})^2$	$(1 - t_{\tilde{p}})(1 + t_{\tilde{p}}^2)$	$(1 - t_{\tilde{p}})(1 + t_{\tilde{p}})^2$
T_2	$(1 - t_{\tilde{p}})^3$	$(1 - t_{\tilde{p}})(1 + t_{\tilde{p}} + t_{\tilde{p}}^2)$	$(1 - t_{\tilde{p}})(1 + t_{\tilde{p}})^2$	$(1 + t_{\tilde{p}})(1 + t_{\tilde{p}}^2)$	$(1 + t_{\tilde{p}})(1 - t_{\tilde{p}})^2$

TABLE V. Weight factors $w_{\tilde{p},r}$ for r traversals of the primitive cycle $\tilde{p}$. These factors allow for symmetry factorizations with repetitions of primitive fundamental cycles.

	E	C_3	C_2	S_4	σ_d
A_1	1	1	1	1	1
A_2	1	1	1	$(-1)^r$	$(-1)^r$
E	2	$2\cos\frac{2\pi r}{3}$	2	$1 + (-1)^r$	$1 + (-1)^r$
T_1	3	$1 + 2\cos\frac{2\pi r}{3}$	$1 + 2(-1)^r$	$1 + 2\cos\frac{\pi r}{2}$	$1 + 2(-1)^r$
T_2	3	$1 + 2\cos\frac{2\pi r}{3}$	$1 + 2(-1)^r$	$(-1)^r + 2\cos\frac{\pi r}{2}$	$2 + (-1)^r$

TABLE VI. Factorizations of $Z(k)$ and weight factors $w_{0,r}$ for the fundamental cycle 0 with ambiguous symmetry classes C_2, σ_d in all subspaces α of the symmetry group T_d.

	C_2, σ_d	$w_{0,r}$
A_1	$(1 - t_0)$	1
A_2	1	0
E	$(1 - t_0)$	1
T_1	$(1 + t_0)$	$(-1)^r$
T_2	$(1 + t_0)(1 - t_0)$	$1 + (-1)^r$

with $\tilde{p}$ the primitive symmetry reduced cycles, r the number of repetitions of it and α the symmetry subspace. A symmetry reduced version of the cycle expansion is obtained by expanding Eq. (27) into a power series in z which is truncated at a maximum cycle length $n_{\max}$. Then, z has to be set to $z = 1$.

D. Harmonic inversion method

The Gutzwiller-Voros zeta function $Z(k)$ in Eq. (27) contains all energy eigenvalues k as complex zeros, and, in principle, it is possible to obtain spectra by a numerical root search. This method has been successfully used for billiards, see e.g. [27]. However, the root search in cycle expansions of high order is numerically expensive. For statistical purposes it is important not to miss any resonances in the strip of the complex plane under consideration. Therefore, a dense grid of initial root guesses has to be used for the root search. Consequently, many resonances will be found several times. Thus, the problem is to distinguish for every new root whether a new distinct resonance has been found or if the new zero has already been computed. As the number of resonances enters into the fractal Weyl law (3) through the counting functions $N(k)$, it is crucial to count individual resonances only once.

An alternative to the computation of zeros is based on the *harmonic inversion method* for high-resolution spectral analysis [31–33]. When Eq. (10) is evaluated along a line of real-valued k or a shifted line $k + \mathrm{i}\delta$ with real k and δ, we obtain a spectrum

$$g(k) = \sum_n \frac{1}{\pi} \frac{\Gamma_n/2 + \delta}{\left(k - \bar{k}_n\right)^2 + (\Gamma_n/2 + \delta)^2} \qquad (28)$$

which is a superposition of resonances with a Lorentzian shape. For negative shifts δ the Lorentzians are located at the positions $\bar{k}_n$, but with reduced widths $\Gamma_n + 2\delta$. The basic idea is now to reformulate, via a Fourier transform, the problem of extracting eigenvalues as a signal processing task. Details of the method are given in [8].

The procedure of calculating quantum spectra is summarized as follows: First, the spectrum $g(k)$ is calculated as a superposition of Lorentzians. We use the cycle-expanded zeta function $Z(k)$ for this purpose. The quantity

$$g(k) = -\frac{1}{\pi} \operatorname{Im} \frac{\mathrm{d}}{\mathrm{d}k} \ln Z(k) = -\frac{1}{\pi} \operatorname{Im} \frac{Z'(k)}{Z(k)} \qquad (29)$$

is evaluated along lines parallel to the real axis with different shifts δ. Thus, the shifts that allow for better results in harmonic inversion enter into the cycle expansion. Then, harmonic inversion is used to obtain the Lorentzians' parameters $\bar{k}_n$ and Γ_n for spectra calculated with different shifts. In the next step, the spectra are filtered via the amplitudes. The quantity $\tilde{g}(k)$ given in (29) should give resonances with an amplitude of $A_n = 1$. True resonances with amplitudes $A_n \approx 1$ can be clearly separated from spurious resonances with nearly zero amplitudes. Finally, the spectra for different shifts δ are joined such that the individual strips do not overlap.

IV. CLASSICAL ESCAPE RATE

The classical escape rate γ_0 can be interpreted descriptively as follows [34]: presume the scattering system un-

der consideration is located in a box much larger than the system itself. Conducting N_0 scattering experiments with the same incident energy k, but different incident directions, one finds that the number N_t of trajectories that are inside the box after the time t has passed decays exponentially as

$$N_t \propto N_0 \, \mathrm{e}^{-\gamma_0 t} \,. \tag{30}$$

The relation of the escape rate and the imaginary part of the quantum resonances can be understood from the correspondence principle. The number of classical trajectories inside the box corresponds to the quantum probability density $\langle \psi | \psi \rangle$. The decay of this probability,

$$\langle \psi | \psi \rangle \propto \mathrm{e}^{-\Gamma t} \,, \tag{31}$$

relates to the decay (30) of the number of classical trajectories inside the box. Thus, in the classical limit

$$\mathrm{Im}\, k_n = -\frac{\Gamma_n}{2} \to -\frac{\gamma_0}{2} \tag{32}$$

holds.

The classical escape rate can be calculated by the method of cycle expansion as well [25]. The escape rate γ_0 is found to be the largest real zero of a dynamical zeta function

$$Z(s) = \prod_{\tilde{p}} (1 - t_{\tilde{p}}(s)) \,, \tag{33}$$

with $\tilde{p}$ the primitive periodic cycles and $t_{\tilde{p}}$ the cycle weights. For a three-dimensional system,

$$t_{\tilde{p}}(s) = \frac{\mathrm{e}^{-l_{\tilde{p}} s}}{\left| \lambda_{\tilde{p}}^{(1)} \lambda_{\tilde{p}}^{(2)} \right|} \,. \tag{34}$$

The quantities $\lambda_{\tilde{p}}^{(i)}$ are the leading stability eigenvalues. A generalization to a zeta function for three dimensions and multiple traversals r of the primitive cycle $\tilde{p}$ is given by

$$Z(s) = \exp\left(-\sum_{\tilde{p}} \sum_r \frac{1}{r} \frac{\mathrm{e}^{-r l_{\tilde{p}} s}}{\left| \lambda_{\tilde{p}}^{(1)} \lambda_{\tilde{p}}^{(2)} \right|^r} \right) \,, \tag{35}$$

with $\lambda_{\tilde{p}}^{(i)}$ the leading two stability eigenvalues of $\tilde{p}$. This zeta function can be cycle-expanded as described in Sec. III. Results for the escape rate γ_0 at various configurations d/R are given in Table VII.

V. RESULTS

The fractal Weyl law has been put to test for billiard systems before. In [6], the 3-disk billiard has been studied. To make our own results comparable to those given in [6], we carry out a similiar discussion.

TABLE VII. Classical escape rates $\gamma_0^{(n)}$ in order n of the cycle expansion for various values of the configuration parameter d/R.

d/R	$\gamma_0^{(1)}$	$\gamma_0^{(2)}$	$\gamma_0^{(3)}$	$\gamma_0^{(4)}$
4	1.16655	1.16459	1.16440	1.16440
6	0.85042	0.84977	0.84974	0.84974
8	0.68259	0.68230	0.68230	0.68230
10	0.57634	0.57619	0.57619	0.57619

A. Defining a scale for the strip widths

For the 3-disk system discussed in [6], the strip widths C have been chosen in relation to the classical escape rate γ_0. For large values $k \to \infty$, the imaginary part of quantum resonances converges to $\mathrm{Im}\, k = -\gamma_0/2$ [6, 35]. Thus, the discussion of the results is simplified by rescaling the strip widths C to

$$\tilde{C} := \frac{C}{\gamma_0/2} \,, \tag{36}$$

which defines a universal scale independent of the symmetry subspace and the ratio d/R. Similar to [6], we evaluate the fractal Weyl law for scaled strip widths $\tilde{C} \in [1; 1.6]$.

B. Counting resonances

We have computed spectra for various values of d/R in all symmetry subspaces. Generally, we find the best convergence behavior of cycle expansions for large values of d/R. Furthermore, the one-dimensional group representations A_1 and A_2 yield the largest number of converged resonances. The two-dimensional representation E and the three-dimensional T_1, T_2 representations converge not as well in cycle expansion since the shadowing of individual cycles is less efficient for the weight factors of these subspaces. For A_1, where all weight factors are equal to 1, the best convergence is observed.

It is important to note that for the tests of the fractal Weyl law we have used only *converged* resonances. For example, the A_1 resonances at $d/R = 10$ are sufficiently converged in the region $\mathrm{Re}\, k < 6000$, $\mathrm{Im}\, k > -0.45$ so that counting functions $N(k)$ obtained in orders 10 and 11 of the cycle expansion fully agree. Thus, comparisons with the fractal Weyl law are not affected by the order of the cycle expansion.

The fractal Weyl law (3) suggests that the counting functions $N(k)$ obey a power law,

$$N(k) \propto k^\alpha \,, \tag{37}$$

thus, in a logarithmic plot of $N(k)$, straight lines of slope $\alpha = 1 + d_\mathrm{H}$ are expected. A sample spectrum and corresponding counting functions for $d/R = 10$ are shown in Fig. 5. This figure is generic in structure, i.e. we have
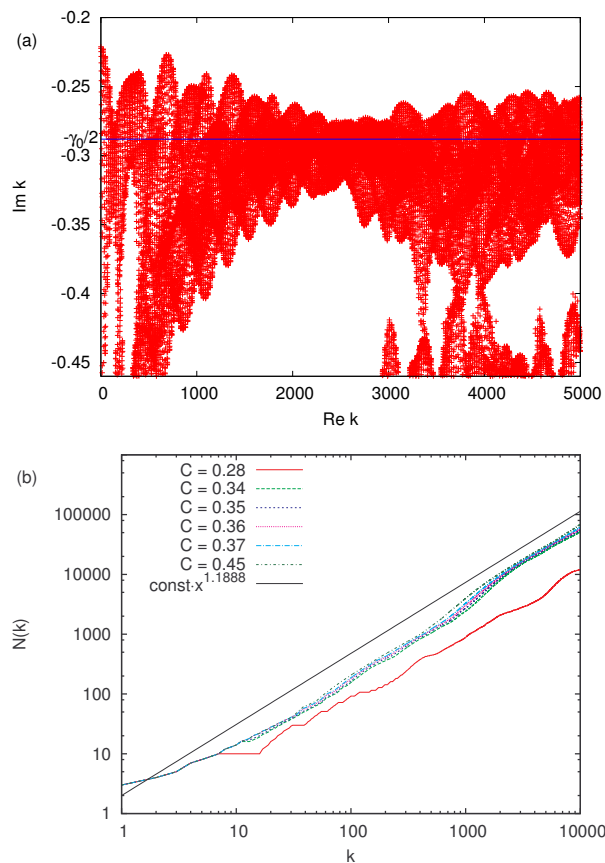
FIG. 5. (a) Spectrum and (b) counting functions $N(k)$ for A_1 resonances calculated from cycle expansion in order 11 for the ratio $d/R = 10$. Several counting functions for different strips C are shown. The curves can be used as "raw data" to fit power laws. In this way, the exponent α in the fractal Weyl law can be obtained and compared to the classical calculations. More than 50 000 resonances have been used in the analysis.

found similar behavior of $N(k)$ in other subspaces and for other ratios d/R as well. Thus, a brief discussion of these features will be given in the following.

We first note that the strip width C has to be sufficiently large, since otherwise, counting would not involve reasonably large numbers of resonances. In the spectrum shown in Fig. 5(a), we have found converged resonances in the relevant strip $\tilde{C} \in [1; 1.6]$ for $\mathrm{Re}\, k \lesssim 6000$. For small strip widths such as $C = 0.28 \Leftrightarrow \tilde{C} = 0.97$, it is evident from Fig. 5(b) that counting involves only a limited number of resonances. Larger strip widths involve more resonances in the counting. However, choosing the strip width too large, the counting may also involve resonances that may not have been converged. Taking the asymptotic behavior of the resonances' imaginary parts into account, choosing rescaled strip widths in the interval $\tilde{C} \in [1.0; 1.6]$ turns out to be a reasonable choice.

Figure 5(b) reveals that the counting functions $N(k)$ deviate from power laws that led to straight lines in the
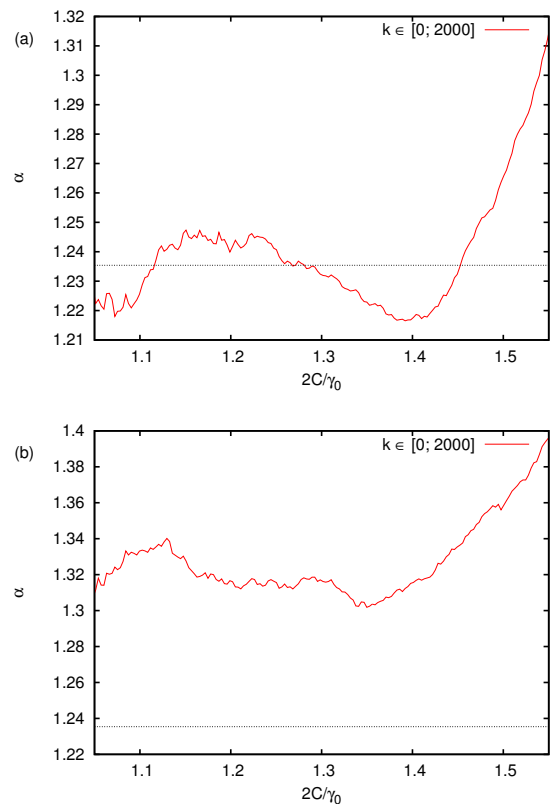

FIG. 6. Exponents α obtained from least-squares fits of a power law to measured counting functions for (a) A_1 resonances and (b) A_2 resonances calculated for $d/R = 6$ in order 13 of the cycle expansion. The power law has been fitted to the interval $k \in [0; 2000]$. The vertical dotted line gives the classical exponent $\alpha = 1 + d_{\mathrm{H}} = 1.2354$.

plot. From this observation one infers that the exponent α will clearly depend on the k-range one fits to. We follow [6] and choose the largest interval converged resonances have been computed for.

C. Putting the fractal Weyl law to test

To provide several tests for the fractal Weyl law, we will provide plots showing the exponents α obtained from least-squares fitting a power function $N(k) \propto k^\alpha$ to the counting functions calculated from the spectra for various subspaces, fitting ranges $[0; k_{\mathrm{max}}]$, configuration parameters d/R and strip widths $\tilde{C}$. We have performed least-squares fits to match the power function (37) to the measured $N(k)$.

1. Configuration $d/R = 6$

For $d/R = 6$, we obtain the exponents shown in Fig. 6. For the A_1 subspace, we find a very good agreement for
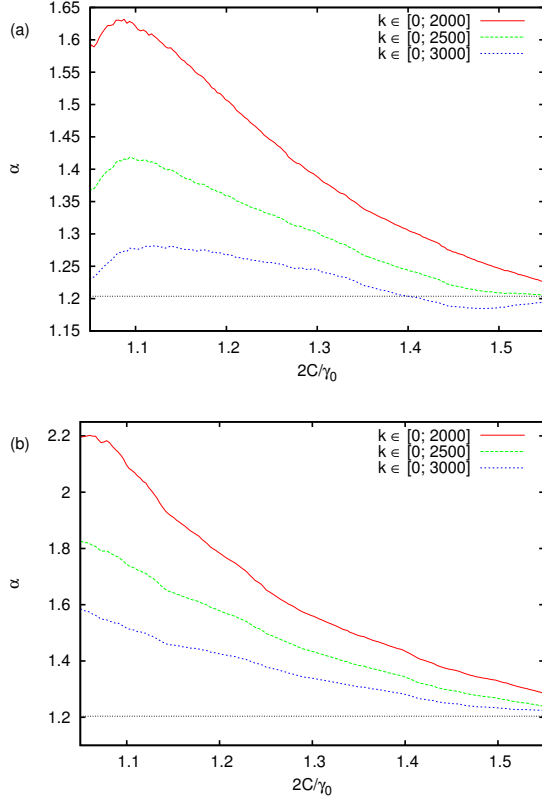
FIG. 7. Exponents α obtained for $d/R = 8$ from least-squares fits of a power law to measured counting functions for (a) A_1 resonances and (b) A_2 resonances. The power law has been fitted to several k-intervals. The vertical dotted line gives the classical exponent $\alpha = 1 + d_{\mathrm{H}} = 1.2063$.
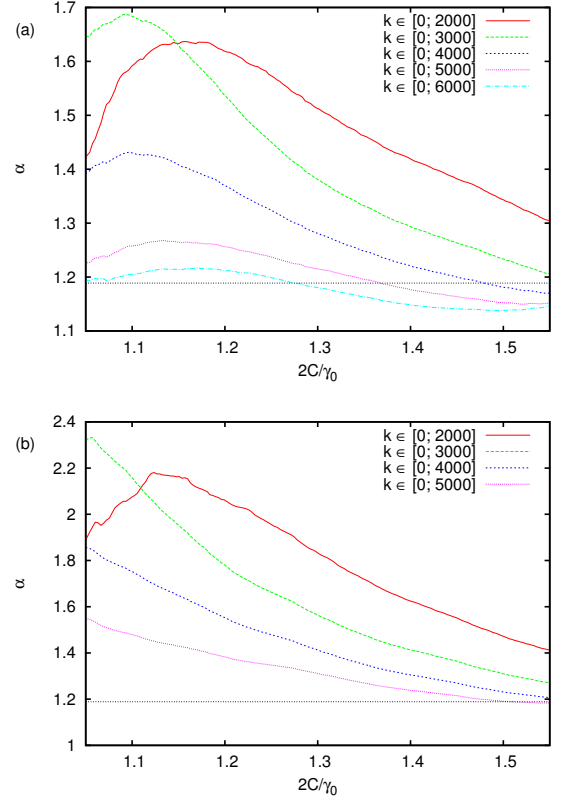

FIG. 8. Exponents α obtained for $d/R = 10$ from least-squares fits of a power law to measured counting functions for (a) A_1 resonances and (b) A_2 resonances. Results for several k-intervals are shown. The vertical dotted line gives the classical exponent $\alpha = 1 + d_{\mathrm{H}} = 1.1888$.

moderate values of $\tilde{C} < 1.4$. The relative error in this $\tilde{C}$-interval is less than 2 percent. However, in the A_2 subspace, all computed exponents are too large by about 8 percent for the same $\tilde{C}$-interval. One possible reason is that the k-range used for fitting is too small.

2. Configuration $d/R = 8$

Performing the same procedure for a configuration parameter of $d/R = 8$, we obtain the plots shown in Fig. 7.

Both plots reveal a clear tendency to obey the fractal Weyl law within a smaller error range when the range of k values used for the fit increases. However, for reasons of convergence, longer spectra have not been used. We note that for $\tilde{C} < 1.4$ and $k \in [0; 3000]$, the error is less than 7 percent for the A_1 resonances. The exponents obtained from A_2 resonances are larger than the expected exponent. For $\tilde{C} = 1.3$, the relative error is about 15 percent.

3. Configuration $d/R = 10$

Finally, the system configuration given by $d/R = 10$ has been studied. Results are shown in Fig. 8.

The counting functions for the A_1 subspace once more tend to give the expected exponent when the k-interval used for the fit increases. For $k \in [0; 6000]$, the error is less than 3 percent. Again, the A_2 spectra yield exponents that are too large. Possibly the k-range investigated here is not large enough to exhibit the asymptotic behavior clearly.

D. Discussion

While the classical calculations for the fractal dimension d_{H} are accurate to at least four significant digits, the agreement of the exponents α is at best 2 to 7 percent for the A_1 spectra. However, we note that for the two-dimensional three-disk billiard, the errors in the exponents are about 5 to 10 percent [6]. Therefore, we conclude that the fractal Weyl law for the four-sphere scattering system is confirmed with roughly the same ac-

curacy as for the three-disk billiard.

A very large k-range seems to be necessary for a proper investigation. This tendency is also visible for the A_2 spectra. The exponents obtained from the A_2 spectra are too large. However, using larger k-intervals, the exponents seem to approach the correct value for large strip widths $\tilde{C}$. Possibly, if larger spectra were available, the expected exponents could be obtained. Unfortunately, we are limited by the convergence of the cycle expansions we use. The higher-dimensional symmetry subspaces E, T_1 and T_2 could not be used to put the fractal Weyl to test law since the spectra did not contain enough converged resonances.

VI. SUMMARY AND OUTLOOK

This paper provides a test of the fractal Weyl law for a three-dimensional scattering system. The four-sphere billiard was investigated both classically and quantum mechanically.

In Sec. II, we have developed a fast and very precise method to gauge the repeller. We found estimates for the Hausdorff dimension d_H with a relative accuracy of 10^{-4}. Although the algorithm is based on strong assumptions, it works over a wider range of the configuration parameter d/R than existing methods.

In Sec. III, we have discussed the methods of semiclassical quantization. We have applied the method of cycle expansion to the four-sphere billiard. Furthermore, for the first time, the method of symmetry decomposition was demonstrated for the Gutzwiller-Voros zeta function of the system.

We have given results in Sec. V. We have provided tests of the fractal Weyl law for various configurations of the system. Although we have found the counting functions $N(k)$ to deviate from power functions, we could confirm the fractal Weyl law for the A_1 resonances of the four-sphere scattering within a small error range. For those spectra we did not find a convincing agreement of calculated level numbers $N(k)$ with the prediction $N(k) \propto k^{1+d_H}$ for, there is hope that larger spectra would lead to the expected exponent. We also assume that the deviations from pure power laws are due to the fact that the energy range under consideration is too small.

As an outlook, the physical origin of the modulations in the counting functions $N(k)$ will have to be investigated. Moreover, it is desirable to study further three-dimensional scattering systems to find out to what extent the results found for the four-sphere billiard carry over and are generic.

[1] H. Weyl, Mathematische Annalen **71**, 441 (1912).
[2] R. Courant, Mathematische Zeitschrift **7**, 1 (1920).
[3] H. P. Baltes and E. R. Hilf, *Spectra of Finite Systems* (B.I. Wissenschaftsverlag, 1976).
[4] J. Sjöstrand, Duke Math. J. **60**, 1 (1990).
[5] M. Zworski, Invent. Math. **136** (1999).
[6] W. T. Lu, S. Sridhar, and M. Zworski, Phys. Rev. Lett. **91**, 154101 (2003).
[7] K. K. Lin and M. Zworski, Chem. Phys. Lett. **355**, 201 (2002).
[8] J. Wiersig and J. Main, Phys. Rev. E **77**, 036205 (2008).
[9] J. A. Ramilowski, S. D. Prado, F. Borondo, and D. Farrelly, Phys. Rev. E **80**, 055201 (2009).
[10] D. L. Shepelyansky, Phys. Rev. E **77**, 015202 (2008).
[11] M. Kopp and H. Schomerus, Phys. Rev. E **81**, 026208 (Feb 2010).
[12] D. Sweet, E. Ott, and J. A. Yorke, Nature **399**, 315 (1999).
[13] D. Sweet, B. W. Zeff, E. Ott, and D. P. Lathrop, Physica D **154**, 207 (2001).
[14] Q. Chen, M. Ding, and E. Ott, Phys. Lett. A **145**, 93 (1990).
[15] A. E. Motter and P. S. Letelier, Phys. Lett. A **277**, 18 (2000).
[16] K. J. Falconer, *The geometry of fractal sets*, Cambridge Tracts in Mathematics, Vol. 85 (Cambridge University Press, Cambridge, 1985).
[17] G. M. Zaslavsky, *Hamiltonian Chaos & Fractional Dynamics* (Oxford University Press, Oxford, 2005).
[18] M. Henseler, A. Wirzba, and T. Guhr, Annals of Physics **258**, 286 (1997).
[19] P. Gaspard and S. A. Rice, J. Chem. Phys. **90**, 2255 (1989).
[20] J. Main, E. Atilgan, H. S. Taylor, and G. Wunner, Phys. Rev. E **69**, 056227 (2004).
[21] M. C. Gutzwiller, *Chaos in Classical and Quantum Mechanics* (Springer, New York, Berlin, Heidelberg, 1990).
[22] A. Voros, J. Phys. A **21**, 685 (1988).
[23] M. Brack and R. K. Bhaduri, *Semiclassical Physics* (Addison-Wesley, Reading, MA, 2003).
[24] P. Cvitanović, Phys. Rev. Lett. **61**, 2729 (1988).
[25] P. Cvitanović and B. Eckhardt, Phys. Rev. Lett. **63**, 823 (1989).
[26] R. Artuso, E. Aurell, and P. Cvitanović, Nonlinearity **3**, 325 (1990).
[27] A. Wirzba, Phys. Rep. **309**, 1 (1999).
[28] H. Primack and U. Smilansky, Phys. Rep. **327**, 1 (2000).
[29] M. Sieber, Nonlinearity **11**, 1607 (1998).
[30] P. Cvitanović and B. Eckhardt, Nonlinearity **6**, 277 (1993).
[31] M. R. Wall and D. Neuhauser, J. Chem. Phys. **102**, 8011 (1995).
[32] J. Main, Phys. Rep. **316**, 233 (1999).
[33] Dž. Belkić, P. A. Dando, J. Main, and H. S. Taylor, J. Chem. Phys. **113**, 6542 (2000).
[34] P. Gaspard and S. A. Rice, J. Chem. Phys. **90**, 2225 (1989).
[35] K. Pance, W. Lu, and S. Sridhar, Phys. Rev. Lett. **85**, 2737 (2000).